The Cryosphere

Discussions

Open Access

EGU

Effects of undercutting and sliding on calving: a coupled approach applied to Kronebreen, Svalbard

Dorothée Vallot[1], Jan Åström[2], Thomas Zwinger[2], Rickard Pettersson[1], Alistair Everett[3], Doug I. Benn[4], Adrian Luckman[5], Ward J. J. van Pelt[1], and Faezeh Nick[6]

[1]Department of Earth Sciences, Uppsala University, Sweden
[2]CSC - IT Center for Science, Espoo, Finland
[3]Norwegian Polar Institute, Norway
[4]School of Geography and Geosciences, University St Andrews, Scotland
[5]Swansea University, Wales, UK
[6] Arctic Geology Department, University Centre in Svalbard, Norway

Correspondence to: Dorothée Vallot

Abstract.

In this paper, we study the effects of basal friction, sub-aqueous undercutting and glacier geometry on the calving process with six different models: a continuum-mechanical ice flow model (Elmer/Ice), a climatic mass balance model, a simple subglacial hydrology model, a plume model, an undercut model and a discrete particle model to investigate fracture dynamics (Helsinki Discrete Element Model, HiDEM). We also demonstrate the feasibility of reproducing the observed calving retreat at the front of Kronebreen, a tidewater glacier in Svalbard, during a melt season. Basal sliding and glacier motion is addressed using Elmer/Ice while calving is modelled by HiDEM. An hydrology model calculates subglacial drainage paths and indicates two main outlets at relatively different rates. Depending on the discharge, the plume model computes frontal melt rates, which are iteratively projected to the actual front of the glacier at subglacial discharge locations. This produces undercutting of different sizes, as melt is concentrated close to the surface for high discharge and is more diffuse for low discharge. By testing different configurations, we show that the geometry (frontal position and topography) controls the calving location while basal sliding controls the calving rate. Undercutting plays a key role in glacier retreat and is necessary to reproduce observed retreat in the vicinity of the discharge location.

1 Introduction

Accelerated discharge of ice into the oceans from land ice is a major contributor to sea level rise, and constitutes the largest source of uncertainty in sea-level predictions for the twenty-first century and beyond (Church et al., 2013). To a large degree, this uncertainty reflects the lack of rigorous methods of predicting ice losses by calving from tidewater glaciers, and associated feedbacks with glacier dynamics.

Recently, it has been suggested that ocean warming could play an important role in determining glacier calving rate and acceleration, by impacting on submarine melt rates (Holland et al., 2008; Luckman et al., 2015). Straneo and Heimbach (2013) proposed two mechanisms responsible for the increase of submarine melt rates at the ice-ocean interface in Greenland: a

warmer and thicker layer of Atlantic water in the fjords and an increase in subglacial discharge mainly during the summer and the autumn. Buoyant meltwater plumes entrain warm ocean water (Jenkins, 2011) and are thought to enhance melt undercutting (Slater et al., 2015) at the ice cliff followed by ice-front collapse. Luckman et al. (2015) investigated controls on seasonal variations in calving rates and showed that calving variations at Kronebreen, the glacier this study focuses on, are best correlated

5   with sub-surface ocean temperature changes linked to melt undercutting of the calving front. However, direct measurements of oceanic properties, ice dynamics, frontal geometries and frontal ablation rates are still too scarce to quantify the relationship between ocean processes, subglacial discharge and ice dynamics and one must rely on modelling. Complex coupled process models can help to gain a better understanding of the physics taking place at tide-water glacier fronts.

In previous modelling work (Van der Veen, 2002; Benn et al., 2007; Amundson and Truffer, 2010; Nick et al., 2010; Cook

10 et al., 2012; Krug et al., 2014, 2015), the dynamics of ice masses have been simulated using continuum models, in which the continuum space is discretized and include processes of mass and energy balance. Continuum models cannot explicitly model fracture and calving processes, but must use simple parameterisations such as damage variables or phenomenological calving criteria. These are largely untested against observations, and may fail to adequately represent key processes. These problems can be circumvented using discrete particle models, which represent ice as assemblages of particles linked by breakable elastic

15 bonds. Åström et al. (2013, 2014) showed that complex crevasse patterns and calving processes observed in nature can be modelled using a particle model, the Helsinki Discrete Element Model (HiDEM). By coupling a continuum model, Elmer/Ice, to a discrete model, HiDEM, we aim to describe the ice successively as a fluid and as a brittle solid. Sliding velocities and ice geometry calculated with the fluid dynamic model are used by the discrete particle model to compute a new calving front position. The effect of subglacial drainage mixing with the ocean during the melt season is taken into account by using a plume

20 model that estimates melt rates at the front according to pro-glacial observed ocean temperatures, subglacial discharge derived from surface runoff and ice front height.

In this paper, we introduce the coupling of the continuum model Elmer/Ice with the HiDEM. We thus harness the ability of HiDEM to model fracture and calving events, while retaining the long-term ice flow solutions of a continuum approach. The aim is to investigate the influence of basal sliding and undercutting at the calving front on calving rate and location. We deter-

25 mine the undercut with a high resolution plume model calculating melt rates from subglacial discharge. The simple hydrology model that calculates the subglacial discharge, is based on surface runoff that is assumed to be transferred directly to the bed and routed along the surface of calculated hydrological potential. We illustrate the approach using data from Kronebreen, a fast-flowing outlet glacier in western Spitsbergen, Svalbard (topography, meteorological and oceanographic data, as well as horizontal surface velocity and front positions from 2013) to assess the feasibility of modelling calving front retreat (rate and

30 position).

2   Study area

Kronebreen is a tidewater glacier situated close to the research station Ny-Ålesund in Svalbard, one of the fastest in the archipelago. The glacier front position undergoes seasonal oscillations, showing advance during the winter and spring followed

by retreat in the summer and autumn. Since 2011, the summer retreat has outpaced the winter advance, with an overall net retreat of ∼2 km between 2011 and 2015 after a relatively stable period since the 1990s (Schellenberger et al., 2015; Luckman et al., 2015; Köhler et al., 2016). Velocities at the front can reach $5\,\mathrm{m\,d^{-1}}$ in the summer with large seasonal and annual variations associated with basal sliding (Vallot et al., 2017).
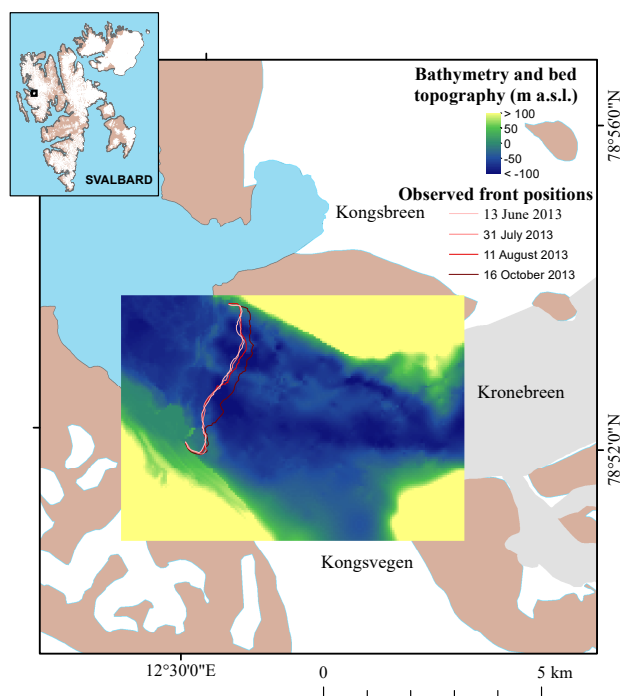
Figure 1. Map of Kronebreen and its surrounding area. The inset map shows the location of Kronebreen in Svalbard with four frontal position of interest. Bathymetry and bed topography are in m a.s.l.

5 The terminus of Kronebreen flows into Kongsfjorden and is characterised by plumes of subglacial discharge, that have been observed along the terminus during the melting season (Trusel et al., 2010; Kehrl et al., 2011; Darlington, 2015; How et al., 2017). There are two main discharge points and the northern plume is generally more active than the southern one. Sediment-rich fresh meltwater discharge is thus mixing with saline fjord waters and can lead to a significant melt rate at the front of the glacier. Large variations of marine processes are typical for arctic fjords and Kongsfjorden seems to experience significant

10 influx of warm water masses during the summer (Cottier et al., 2005) as shown by (Nahrgang et al., 2014) presenting ocean temperatures of Kongsfjorden from moored observatories in 2012-2013. From October to mid-November 2012, the whole water column temperature is warm (4-5 °C). Thereafter, the upper 100 m become colder and in January 2013, the whole water column temperature drops to 1-3 °C. From March to May, it approaches 0 °C and starts to increase again in May (1-3 °C). In August, the temperature has reached 3-4 °C and the upper 100 m increase particularly to reach 5-6 °C towards the end of

15 the season. Fjord bathymetry (Howe et al., 2003; Aliani et al., 2016) and bed topography under the glacier systems have been
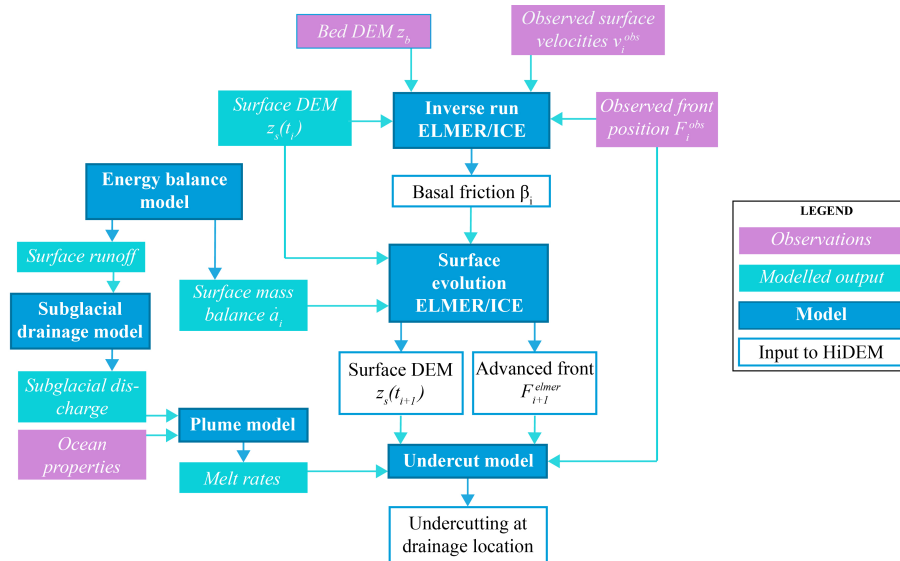
Figure 2. Model scheme presenting the calculation of the sliding and geometry (Elmer/Ice) as well as the undercutting at the subglacial discharge as input to the glacier calving from the HiDEM.

collected by (Lindbäck et al., 2017) and reveal a glacier terminus height of about $150\,\mathrm{m}$ at the discharge locations with $100\,\mathrm{m}$ of submerged column (see Fig. 1). Close to the subglacial discharge locations, a changing grounding-line fan of sediments has been observed (Trusel et al., 2010) potentially ensuring a pinning point if the glacier were to advance in the future. Luckman et al. (2015) showed that calving rates are strongly correlated with subsurface fjord temperatures, indicating that the dominant control on calving is melt undercutting, followed by collapse of the sub-aerial part.

3 Methods

3.1 Observed surface velocities and front positions

Ice surface velocities were derived from feature tracking of TerraSAR-X image pairs in slant range using correlation windows of $200{\times}200\,\mathrm{pixels}$ at every $20\,\mathrm{pixels}$, and subsequently ortho-rectified to a pixel size of $40\,\mathrm{m}$ using a digital elevation model (Luckman et al., 2015). Acquisition is done roughly every $11\,\mathrm{days}$ for the period May-October 2013. Uncertainties in surface velocity are estimated to be $\sim 0.4\,\mathrm{m\,d^{-1}}$, and comprise a co-registration error ($\pm\,0.2\,\mathrm{pixels}$) and errors arising from unavoidable smoothing of the velocity field over the feature-tracking window. Ice-front positions were manually digitised from the same images used for feature tracking after they had been orthorectified to a pixel size of 2m using a surface DEM Luckman et al. (2015).

3.2 One-way coupling approach

We use surface velocity and frontal position described above to test the effects of sliding and undercutting on calving by coupling different models. This one-way coupling approach is divided into three parts using six models (see Fig. 2): computing sliding and geometry (with Elmer/Ice), determining of undercutting (with energy balance model, subglacial hydrology model, plume model and undercutting model) and computing calving (with HiDEM). We first infer sliding from surface velocities using an adjoint inverse method implemented in Elmer/Ice with an updated geometry from observations at different time steps.

Table 1. Time step and associated date.

Time step t_i	Date	Comment
t_0	2 June 2013	Before the onset of the melting season
t_1	13 June 2013	First melt
t_2	24 June 2013	
t_3	5 July 2013	
t_4	31 July 2013	Period of high surface runoff
t_5	11 August 2013	
t_6	22 August 2013	Minimum basal friction
t_7	2 September 2013	
t_8	13 September 2013	
t_9	24 September 2013	
t_{10}	5 October 2013	
t_{11}	16 October 2013	After the last melt

We set t_0 at the velocity acquisition just before the first melt and the following time steps are set at each observation of surface velocity. The exact dates are summarized in Table 1.

At each iteration, corresponding to an observed front position, the front and the surface are dynamically evolving to the next front position observation time iteration (roughly 11 days). Second, given subglacial drainage inferred from modelled surface runoff, a plume model calculates melt rates based on the subglacial discharge for each iteration, which are subsequently applied to the front geometry at subglacial discharge locations. At each iteration, the front geometry takes into account the undercut modelled at the former iteration. Finally, the sliding, geometry and undercut are taken as input to the calving particle model HiDEM for each iteration.

We call this approach a one-way coupling because inputs to the HiDEM are output results from Elmer/Ice but not vice versa. A completely coupled physical model would calculate the basal friction from a sliding law rather than an inversion. We therefore chose to first study the effect of sliding before performing a full coupling. In principle, such an implementation is possible using the same steps as this study.

3.3 Sliding and frontal advance with continuum model Elmer/Ice

At the base of the glacier, we use a linear relation for sliding law of the form

$$\tau_b + \beta u_b = 0, \tag{1}$$

with τ_b, the basal shear stress and u_b, the basal velocity. The basal friction coefficient, β, is optimized to best reproduce observed velocity distribution at the surface of the glacier (Vallot et al., 2017). That is done by using the self-adjointness of the Stokes equations for an inversion (Gagliardini et al., 2013). The inversion is performed using the method of Lagrange multipliers to minimise a cost function including the observed horizontal surface velocities and a Tikhonov regularisation (Vallot et al., 2017).
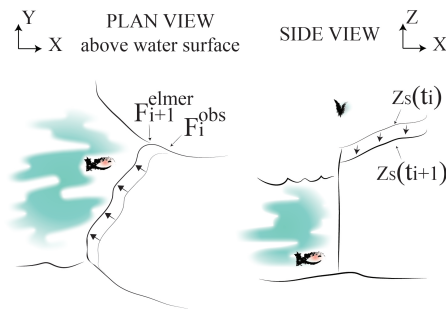
Figure 3. Front position and surface elevation changes with Elmer/Ice during $\Delta t = t_{i+1} - t_i$.

The bed topography, z_b, is derived from profiles of airborne and ground-based common-offset ice penetrating radar surveys distributed over Kronebreen (Lindbäck et al., 2017). The initial surface topography includes different available surface DEMs. After each inversion, the temporal evolution of the glacier is mathematically described by the kinematic boundary condition defined at the surface,

$$\frac{\partial z_s}{\partial t} + u_x(z_s)\frac{\partial z_s}{\partial x} + u_y(z_s)\frac{\partial z_s}{\partial y} - u_z(z_s) = \dot{a}_s(t_i), \tag{2}$$

which describes the evolution of the free surface elevation, $z = z_s$, in reaction to a given net accumulation, $\dot{a}_s(t_i)$, calculated using a coupled modelling approach after Van Pelt and Kohler (2015), described in the next section.

The front position is also able to advance and we will call $F_i^{obs}(z = 0)$, the front position observed at time t_i with $z = 0$ at the sea level and $F_{i+1}^{elmer}(z = 0)$, the advanced modelled front position after $\Delta t = t_{i+1} - t_i$ (see Fig. 3).

3.4 Surface runoff and subglacial discharge model

The surface mass balance, $\dot{a}_s$, and runoff are simulated with a coupled energy balance - snow modelling approach (Van Pelt and Kohler, 2015). The coupled model solves the surface energy balance to estimate the surface temperature and melt rates. The subsurface routine simulates density, temperature and water content changes in snow and firn while accounting for melt water percolation, refreezing and storage. The model is forced with 3-hourly meteorological time-series of temperature, precipitation, cloud cover and relative humidity from the Ny-Ålesund weather station (eKlima.no; Norwegian Meteorological Institute). Elevation lapse rates for temperature are calculated using output from the Weather Research and Forecast (WRF) model Claremar et al. (2012), while the precipitation lapse rate is taken from (Van Pelt and Kohler, 2015); zero lapse rates are assumed for cloud cover and relative humidity.

The temporal subglacial discharge at the calving front is estimated from integration of daily surface runoff assumed to be directly transferred down to the glacier bed. Assuming the basal water pressure at over burden, the flow path of the melt-water towards the glacier front is determined from the hydraulic potential surface defined as

$$\phi = \rho_i g(z_s - z_b) + \rho_w g z_b, \tag{3}$$

with g, the gravitational acceleration. The flow path along the bed surface is determined by D-infinity flow method where the flow direction from a grid cell is defined as the steepest triangular facets created from the 8-neighboring grid cells (Tarboton et al., 1987). The flow from the center grid cell is distributed proportionally to the two cells that define the steepest facet. The flow is accumulated as the melt water is routed along the calculated hydraulic surface towards the front and outlet points at the front are determined by identifying flow rates higher than $1\,\mathrm{m^3\,s^{-1}}$. The hydraulic potential surface is filled before flow accumulation is calculated to avoid sinks.

3.5 Plume model and submarine melt rates

A high-resolution plume model is used here to simulate the behaviour of subglacial discharge at the terminus of Kronebreen. The model is based upon the fluid dynamics code Fluidity (Piggott et al., 2008) which solves the Navier-Stokes equations on a fully unstructured three-dimensional finite element mesh. The model formulation builds upon the work of Kimura et al. (2013), with the addition of a large eddy simulation (LES) turbulence model (Smagorinsky, 1963) and the use of the synthetic eddy method (SEM) at the inlet (Jarrin et al., 2006).

The geometry of the model is adapted to Kronebreen by setting the water depth to $100\,\mathrm{m}$ and initialising the model with ambient temperature and salinity profiles collected from ringed seals instrumented with GPS-equipped Conductivity, Temperature and Depth Satellite Relay Data Loggers (GPS-CTD-SRDLs) (Boehme et al., 2009; Everett et al., 2017). These data were collected between 14th August and 20th September 2012 from a region between one and five kilometres from the glacier terminus and are taken as representative of the ambient conditions in the fjord during summer. Melt rates are calculated on the terminus using a three-equation melt parameterisation described by Jenkins and Bombosch (1995) and McPhee et al. (2008) and implemented in Fluidity by Kimura et al. (2013). Velocities driven by ocean circulation are typically around 2-3 orders of magnitude smaller than plume velocities and therefore neglected.

The Cryosphere
Discussions

The model is spun-up until the turbulent kinetic energy in the region of the plume reaches a steady state and thereafter run for 10 minutes of steady-state model time. Melt rates are extracted from the duration of the steady-state period, then time averaged and interpolated onto a uniform $1 \times 1\,\mathrm{m}^2$ grid covering a 400-m-wide section of the glacier terminus.

The high-computational cost of the model means that it cannot be run continuously over the study period, nor can the full range of discharges and oceanographic properties be tested. Instead, representative cases M_d using uniform ambient ocean properties and discharges d of 1, 10, 50 and $100\,\mathrm{m}^3\,\mathrm{s}^{-1}$ were tested and the melt rate profiles for intermediate discharges were linearly interpolated from these cases.

3.6 Undercutting model

We assume a vertically aligned surface front at the beginning of the melt season. We know the position of the front, $F_0^{obs}(z=0)$, at each passage of the satellite. The front is spatially digitized with $10\,\mathrm{m}$ spacing. Sea level is situated at $z=0$.
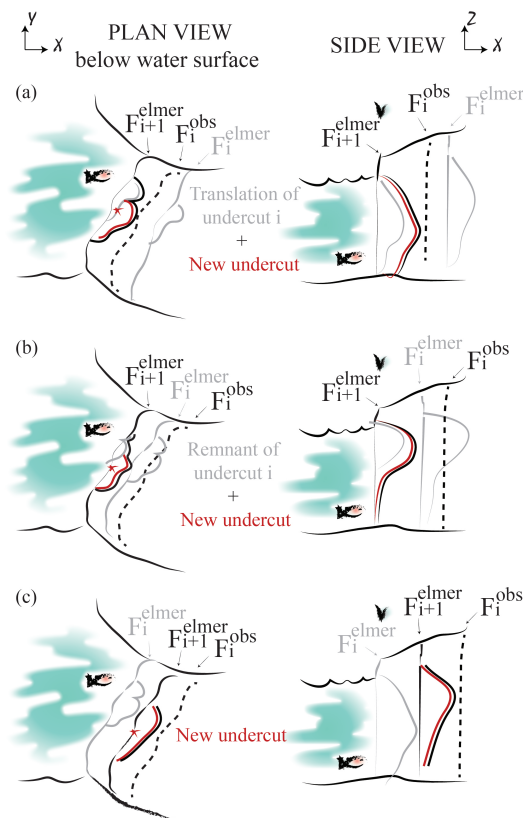
Figure 4. Three cases of former undercut position at z relative to $F_i^{obs}(z=0)$. The red star represents the discharge location. **(a)** $F_i^{obs}(z=0)$ is behind $F_{i+1}^{elmer}(z=0)$ and in front of $F_i^{elmer}(z)$. The undercut from $F_i^{elmer}(z)$ is translated to $F_{i+1}^{elmer}(z)$ (gray color) and the new undercut is superposed (red color). **(b)** $F_i^{obs}(z=0)$ is in front of $F_i^{elmer}(z)$. The remnant from $F_i^{elmer}(z)$ (what is behind $F_i^{obs}(z=0)$) is translated to $F_{i+1}^{elmer}(z)$ (gray color) and the new undercut is superposed (red color). **(c)** $F_i^{obs}(z=0)$ is behind $F_i^{elmer}(z)$. The undercut from $F_i^{elmer}(z)$ is ignored and the undercut created at t_{i+1} is the only one (red color).

When the first discharge occurs, the melt rate calculated with the plume model in 2D is summed for the period of time between t_0 and t_1 and projected to the front $F_1^{elmer}(z = 0)$ at the location of the subglacial outlets and ice is removed normal to the front. This yields a new position of the front at depth z below sea level called $F_1^{elmer}(z)$. At time t_i, the front position at depth z is $F_i^{elmer}(z)$. Three different cases, depending on the relative position of the observed and modelled fronts, are then possible as shown in Fig. 4:

– if the new observed position $F_i^{obs}(z = 0)$ is behind $F_i^{elmer}(z = 0)$ and in front of $F_i^{elmer}(z)$, the melted undercut is kept and advances in the flow direction the same distance as the surface modelled front $F_{i+1}^{elmer}(z = 0)$ (see Fig. 4a),

– if the new observed position $F_i^{obs}(z = 0)$ is in front of $F_i^{elmer}(z)$, the undercut is displaced to the next modelled front $F_{i+1}^{elmer}(z = 0)$ (see Fig. 4b),

– if the new observed position $F_i^{obs}(z = 0)$ is behind $F_i^{elmer}(z)$, the front starts from a vertical profile again (see Fig. 4c).

The melt summed up between t_i and t_{i+1} is then applied to $F_i^{elmer}(z)$ to obtain $F_{i+1}^{elmer}(z)$ and so on. Melt above the surface has not been taken into account so that the effect of submerged ice feet, regarded as a third order process by Benn et al. (2007), is not described. The bed topography, the new geometry (surface elevation, front position with or without undercut) and the basal friction are then interpolated onto a 10×10 m grid to feed the HiDEM and a new front, F_{i+1}^{hidem} is modelled by calving.

3.7 Calving with first-principles ice fracture model HiDEM

The fracture dynamics model is described in detail in Åström et al. (2014, 2013). This first-principles model is constructed by stacking blocks connected by elastic and breakable beams representing discrete volumes of ice. For computational efficiency, we use a block size of 10 m.

At the beginning of a fracture simulation, the ice contains a few randomly distributed broken beams with no internal stresses, representing small pre-existing cracks in the ice. The dynamics of the ice is computed using a discrete version of Newton's equation of motion, iteration of time steps and using inelastic potentials for the interactions of individual blocks and beams. As the ice deforms under its own weight, stresses on the beams increase, and if stress reaches a failure threshold the beam breaks and the ice blocks become disconnected but continue to interact as long as they are in contact. In this way cracks in the ice are formed. For computational reasons, we initialise the glacier using a dense packed face-centered cubic (fcc) lattice of spherical blocks of equal size. This introduces a weak directional bias in the elastic and fracture properties of the ice. The symmetry of the underlying fcc-lattice is however easily broken by the propagating cracks. The ground under the ice or at the sea-floor is assumed to be elastic with a linear friction law that varies spatially (Eq. 1).

The time step is limited by the travel time of sound waves through a single block and is thereby set to 10^{-4} sec. If the stress in the ice exceeds a fracture threshold, crevasses will form and ice may calve off the glacier. The duration of a typical calving event at Kronebreen is a few tens of seconds followed by a new semi-equilibrium when the ice comes to rest. As HiDEM cannot be triggered too often because of computational limitations, we simulate ice flow with Elmer/Ice and compute calving with HiDEM thereafter. Calving events will then appear as fewer but bigger events compared to observations.

The basal friction coefficients, β, at the front of Kronebreen are in the order of 10^8-$10^{12}\,\mathrm{kg\,m^{-2}\,s^{-1}}$ (Vallot et al., 2017) and to avoid instabilities to build up, a cut-off value, above which particles are assumed to be stuck to the bed substrate, is fixed at $\beta = 10^{12}\,\mathrm{kg\,m^{-2}\,s^{-1}}$.

When simulating with an undercut at discharge location and in order to avoid complication in the HiDEM, we remove particles below the maximum melt (no ice foot).

In the ocean, the basal friction coefficient is taken equal to the mean of the values at the terminus in case the ice advances. Due to the very high bed friction, hardly any sliding motion would take place during the few minutes of a HiDEM simulation, which will affect the calving behaviour. Because of the different time scales of calving and sliding processes, it is however possible to scale down the friction some orders of magnitude while still maintaining the separation of time-scales. Sliding is therefore scaled down to roughly correspond to a HiDEM simulation physical time, which better represents the time-scale separating non-negligible calving events at Kronebreen.

An ice block is calved when all bounds are broken from the main piece of ice even though it does not separate from the front.

In a fully coupled model, the altered ice geometry after calving could then be re-implemented in the flow model, acting as the initial state for a continued prognostic simulation with the continuum model. Here, this back-coupling is replaced by prescribing the next configuration obtained by satellite.

3.8 Frontal ablation calculation

The frontal ablation rate at the water margin at time t_i, $\dot{a}_c(t_i)$, is the difference between the ice velocity at the front, $u_w(t_i)$ and the rate of change of the frontal position, $\partial L/\partial t$ integrated over the terminus domain Γ_w as defined in McNabb et al. (2015). This yields

$$\dot{a}_c(t_i) = \int_{\Gamma_w} u_w(t_i) - \frac{\partial L}{\partial t}\,\mathrm{d}\Gamma_w, \tag{4}$$

with

$$\int_{\Gamma_w} \frac{\partial L}{\partial t}\,\mathrm{d}\Gamma_w = \frac{\Delta A(t_i)}{t_i - t_{i-1}} \int_{z_{\Gamma_w}} \mathrm{d}z \tag{5}$$

and $\Delta A(t_i)$, the area change at the terminus over the time $t_i - t_{i-1}$. We want to compare the ablation rates from F_i^{elmer} for observed and modelled cases. For the observed case, the ablation rate is calculated between the advanced front F_i^{elmer} and the observed front F_i^{obs}. For the modelled case, the ablation rate is calculated between F_i^{elmer} and the modelled front F_i^{hidem}. The total subaqueous melt rate, $\dot{a}_m$, at the front of the glacier is omitted in this balance.

3.9 Calving scenario simulations

We investigate the effect of three different parameterisations on calving activity: the geometry (g_i) corresponding to the frontal position and topography, the sliding velocity mainly influenced by the basal friction parameter (β_i) and the undercut at subglacial discharge (u_i) for four distinctive times $t_i = \{t_0, t_4, t_6, t_{11}\}$ (see Table 1). The different configurations are referred as

$C(g_i, \beta_j, u_i)$ with $i, j \in [0, 4, 6, 11]$. If $u_i = 0$, there is no undercut, hence a vertical ice front at the subglacial discharge. At $t = 0$, the melt season has not started yet so there is no modelled undercut. At $t = 11$, the melt season is finished and there is no modelled undercut. If $j \neq i$, the geometry, g_i, is taken at t_i and the basal friction, β_j, at t_j to assess the roles of geometry and basal sliding. We investigate basal friction at t_0 and t_6 since the former has maximum friction and the latter minimum friction of the studied cases. The configuration studied in this paper are summarised in Table 2.

**Table 2.** Different configurations, C_k, characteristics and periods.

Configuration	Characteristics	Applied to
$C(t_i, \beta_i, 0)$	Geometry at t_i Sliding at t_i Vertical front	$i \in [0, 4, 6, 11]$
$C(t_i, \beta_i, u_i)$	Geometry at t_i Sliding at t_i Undercut at discharge	$i \in [4, 6]$
$C(t_i, \beta_j, 0)$	Geometry at t_i Sliding at t_j Vertical front	$(i, j) \in [(0, 6)$ $, (6, 0)]$

4 Results

4.1 Basal friction coefficients

The basal friction coefficient, β, for the four runs presented above, is shown in Fig. 5. At t_0, before the melt season, the basal friction is high and roughly homogeneous over the first kilometer. At t_4, when the surface runoff is the highest, the pattern is similar but with a large offset. The lowest friction is reached at t_6, particularly at the front and in the southern part of the glacier. The highest friction is reached at t_{11} a kilometer from the front. Close to the front position, however, the friction is still high.
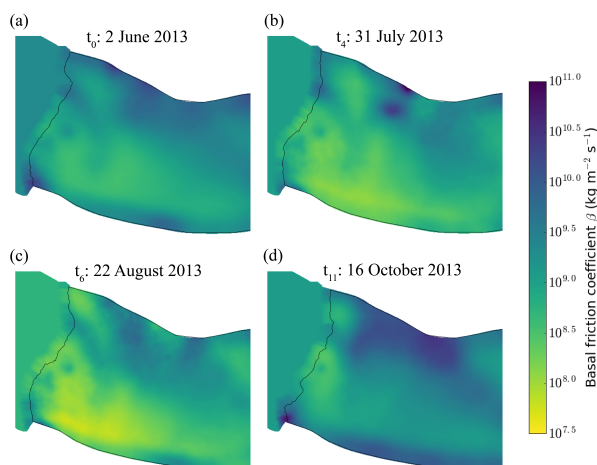
Figure 5. Basal friction coefficient and observed frontal position for **(a)** t_0: 2 June 2013, **(b)** t_4: 31 July 2013, **(c)** t_6: 22 August 2013 and , **(d)** t_{11}: 16 October 2013.

4.2 Subglacial discharge and submarine melt rates

The hydrological model predicts that there are two main subglacial channels exceeding a discharge of $1\,\mathrm{m^3\,s^{-1}}$ of water (see Fig. 6a). This is in accordance with satellite images showing upwelling (Trusel et al., 2010; Kehrl et al., 2011; Darlington, 2015; How et al., 2017). Surface melt and consequently assumed discharge at the northern outlet - in short Northern Discharge

5 (ND) - starts June 6 and ends October 1 while the discharge at the southern outlet (SD) starts June 21 and ends August 22. Fluxes at ND clearly exceed those at SD as shown in Fig. 6b and Table 3.
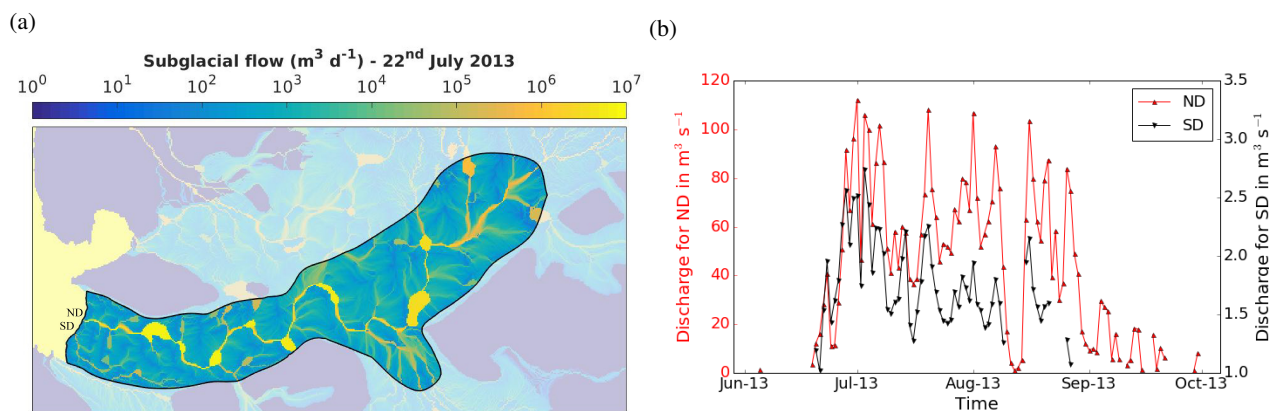

Figure 6. (a) Subglacial flow following the hydraulic potential surface (in $\mathrm{m^3\,d^{-1}}$) in logarithmic scale on the 22nd July 2013. **(b)** Daily discharge for the northern and southern discharge (ND and SD respectively) during the melting season (data gaps corresponds to no discharge).

Table 3. Total volume of subglacial discharge modelled per period of calving front recording.

Start date	End date	Days	Volume (m^3)	
			ND	SD
2 Jun (t_0)	13 Jun (t_1)	11	1.27e5	
13 Jun (t_1)	24 Jun (t_2)	11	8.73e6	4.94e5
24 Jun (t_2)	5 Jul (t_3)	11	6.24e7	2.05e6
5 Jul (t_3)	31 Jul (t_4)	26	1.10e8	3.54e6
31 Jul (t_4)	11 Aug (t_5)	11	6.2e7	1.36e6
11 Aug (t_5)	22 Aug (t_6)	11	4.69e7	1.04e6
22 Aug (t_6)	2 Sept (t_7)	11	3.91e7	2.03e5
2 Sept (t_7)	13 Sept (t_8)	11	1.18e7	
13 Sept (t_8)	24 Sept (t_9)	11	6.20e6	
24 Sept (t_9)	5 Oct (t_{10})	11	8.04e5	

The melt rate profiles calculated by the plume model for four different volumes of subglacial discharge are shown in Fig. 7.
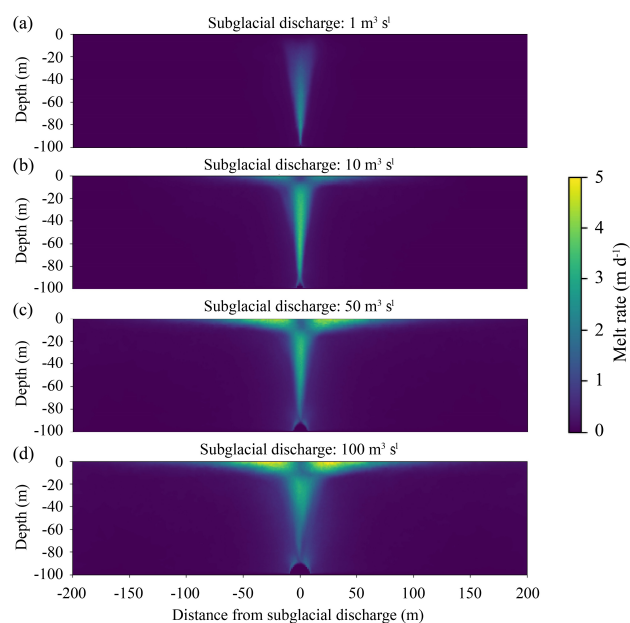
Figure 7. Melt rates, M_d, from the plume model given a discharge, d, of (a) $1\,\mathrm{m^3\,s^{-1}}$, (b) $10\,\mathrm{m^3\,s^{-1}}$, (c) $50\,\mathrm{m^3\,s^{-1}}$ and (d) $100\,\mathrm{m^3\,s^{-1}}$.

At a discharge of $1\,\mathrm{m^3\,s^{-1}}$, melt rates are low ($< 2.5\,\mathrm{m\,d^{-1}}$) with the maximum melt rate occurring at depth and negligible melt rates close to the water line. At $10\,\mathrm{m^3\,s^{-1}}$, the melt profile reaches the surface and has highest melt rates ($\sim 3.5\,\mathrm{m\,d^{-1}}$) along the plume column. With $50\,\mathrm{m^3\,s^{-1}}$ and $100\,\mathrm{m^3\,s^{-1}}$ discharge, the highest melt rates are attained at the ocean surface on
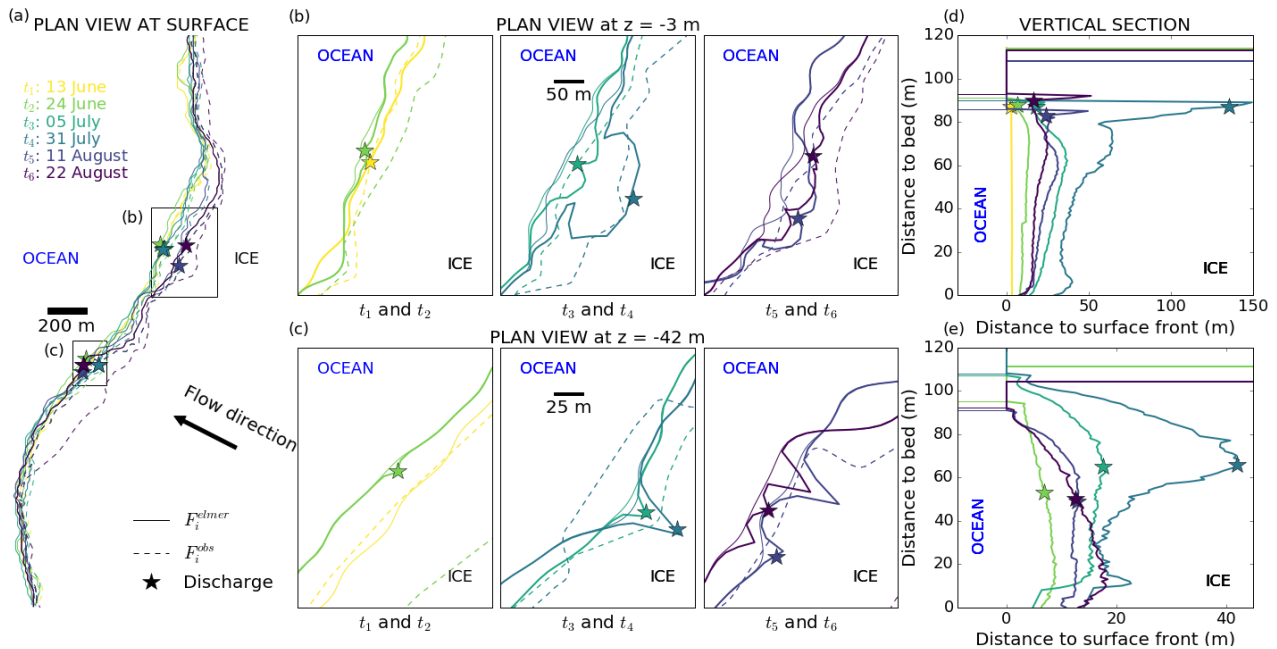
Figure 8. **(a)** Plan view of the frontal position of Kronebreen at six different dates, defined by different colors, corresponding to the satellite data acquisition dates during the melting season in 2013 (up to the 22nd of August). At t_i, the observed front, F_i^{obs}, is represented by a dashed line and the advanced front, $F_i^{elmer}(z = 0)$, by a thin line. The discharge location is defined by a star. Enlargement at **(b)** the northern discharge (ND) area at $z = -3\,\text{m}$ and at **(c)** the southern discharge (SD) area at $z = -42\,\text{m}$ with the advanced front at depth z where undercut has been applied, $F_i^{elmer}(z)$, represented by a thick line. Vertical section **(d)** at the northern discharge (ND) location and at **(e)** the southern discharge (SD) location. The stars in (d,e) indicate the plan view elevation z from (b,c).

the sides of the plume column ($\sim 5\,\text{m}\,\text{d}^{-1}$ and $\sim 6\,\text{m}\,\text{d}^{-1}$ respectively). In general, low discharges drive maximum melt within the plume and at depth, while higher discharges drive stronger surface gravity currents, and therefore gives higher melt rates at the surface.

4.3 Undercutting

5 The modelled frontal position is summarised in Fig. 8 in plan view and vertical view at the discharge locations. In most cases for the ND location, where the discharge is the highest, the melt profile (Fig. 8d) creates an undercut profile concentrated right near the waterline. Fried et al. (2015) found similar results when modelling shallow grounding lines (100-250 m) plume model melt given $250\,\text{m}^3\,\text{s}^{-1}$ discharge. It is interesting to see that the observed front after calving, F_i^{obs}, (dashed line in Fig. 8a-b) generally falls behind the undercutted front before calving, $F_i^{elmer}(z)$, (thick line in Fig. 8b).

10 The frontal submerged undercut driven by the plume differs in shape from one location to another. The melting at the SD is smoother from the surface to approximately 50 m depth and is also lower than ND (Fig. 8c-e). where the discharge is the highest, the melt rate peaks just below the waterline and stetching laterally from the vertical centerline of the plume but low

at depth. At the SD, melting is strongest at depth due to lower discharge rates. One should keep in mind that this approach neglects the change of the front during the period of interest (11 days for most cases). In reality, calving would occur more often during that period, making such large undercuts, as the modelled ones, not possible. This simplification has consequences for the next step when the particle model handles the calving of icebergs due to front imbalance.
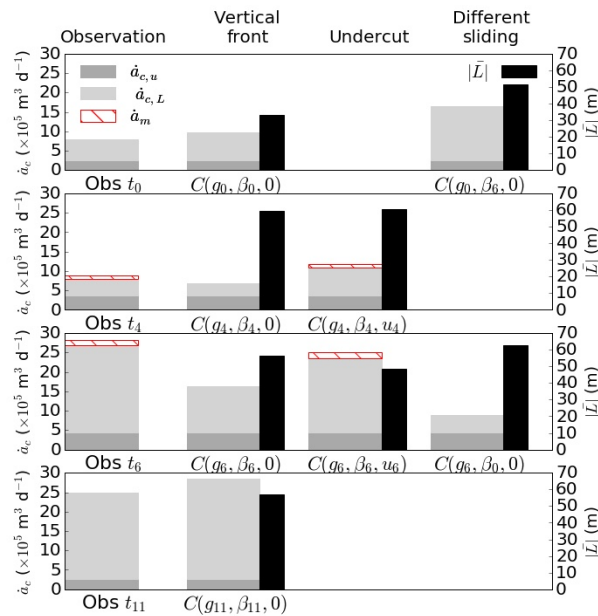
5 4.4 Observed calving rates and modelled calving

The observed calving rate averaged over the entire calving front volume of ice, $\dot{a}_c^{obs}$ is the difference between the frontal velocity, $u_w^{obs}(t_i)$, and the rate of position change, $\partial L^{obs}/\partial t$ integrated over the terminus domain. These quantities and the total modelled ice mass melted by the plume normalised per day (when an undercut is prescribed) are given in Table 4.

Table 4. Observed calving rate, $\dot{a}_c^{obs} = \dot{a}_{c,u}^{obs} - \dot{a}_{c,L}^{obs}$, in $10^5 \, \mathrm{m}^3 \, \mathrm{d}^{-1}$, as the difference between the tangential ice velocity at the front and the rate of change of the frontal position integrated over the terminus domain, and modelled subaqueous melt rate, $\dot{a}_m$, in $10^5 \, \mathrm{m}^3 \, \mathrm{d}^{-1}$.

		t_0	t_4	t_6	t_{11}
$\dot{a}_c^{obs}$	$\dot{a}_{c,u}^{obs}$	2.63	3.68	4.31	2.56
	$\dot{a}_{c,L}^{obs}$	−5.30	−4.28	−22.63	−22.43
	Total	7.93	7.97	26.94	24.99
$\dot{\mathrm{a}}_{\mathrm{m}}^{\mathrm{obs}}$	**SD**		0.08	0.14	
	ND		0.86	1.25	
	Total		0.94	1.39	
Ratio $\dot{\mathrm{a}}_{\mathrm{m}}/\dot{\mathrm{a}}_{\mathrm{c}}$			*11.8 %*	*5.2 %*	

10 To assess the performance of the pseudo-coupling, we evaluate the calving rate averaged over the entire calving front volume of ice (see Eq. 4), and the mean absolute distance between the modelled and the observed front, $|\bar{L}|$. These are presented in Fig. 9 for each configuration as well as the observed calving rate.

Figure 9. Observed and modelled calving rate, $\dot{a}_c$, in $\mathrm{m^3\,d^{-1}}$ is presented as the integrated tangential ice front velocity $\dot{a}_{c,u}$ (dark gray), the integrated rate of change of the frontal position, $\dot{a}_{c,L}$ (light gray) and the total subaqueous melt rate, $\dot{a}_m$ (hashed red) if an undercut is prescribed for each configuration. The mean distance difference between the modelled and the observed front, $|\bar{L}|$ is in black.

Fig. 10 shows the different front positions after the HiDEM simulation for each configuration of the studied time. Fig. 11 shows strain rates modelled by HiDEM that resemble a crevasse pattern (yellow lines representing crevasses).

At t_0, before the melt started, the front has retreated at a rate of $7.93 \times 10^5\,\mathrm{m^3\,d^{-1}}$ with a frontal ice flux of $2.63 \times 10^5\,\mathrm{m^3\,d^{-1}}$, mostly in the middle part with a calved area of $5.1 \times 10^4\,\mathrm{m^2}$. The HiDEM produces a slightly higher calving rate, $9.76 \times 10^5\,\mathrm{m^3\,d^{-1}}$

5 with a vertical ice front configuration (red line $C(g_0, \beta_0, 0)$ in Fig. 10a) at a mean distance of $32\,\mathrm{m}$ from the observed front. However, calving is concentrated south of SD in a zone of high ice velocity and high strain rates as modelled by HiDEM (see Fig. 11).

With peak surface runoff, at t_4, the observed calving rate equals $7.97 \times 10^5\,\mathrm{m^3\,d^{-1}}$, similar to t_0 but with higher ice velocities ($3.68 \times 10^5\,\mathrm{m^3\,d^{-1}}$). Observed retreat at the ND location and north of it is significant but is not reproduced by the configuration

10 with a vertical ice front (red line $C(g_4, \beta_4, 0)$ in Fig. 10b). Instead the front is retreating south of SD in the same fashion as for t_0. The calving rate ($6.82 \times 10^5\,\mathrm{m^3\,d^{-1}}$) is therefore close to the observed value, but the mean distance between the observed and the modelled front is close to $60\,\mathrm{m}$ (see Fig. 9). For the undercut configuration (blue line $C(g_4, \beta_4, u_4)$ in Fig. 10b), the calving rate is also overestimated at the same location but the observed retreat around ND is matched by the HiDEM. The mass removed by undercutting represents $11.8\,\%$ of the total observed calving rate (see Table 4) and is therefore non-negligible.

15 At the SD, the observed front is advancing (see Fig. 8b) and regardless of the applied modelled front configuration (with or without undercut), a similar slight retreat is modelled. In this case, the undercut has no influence on the calving.

16
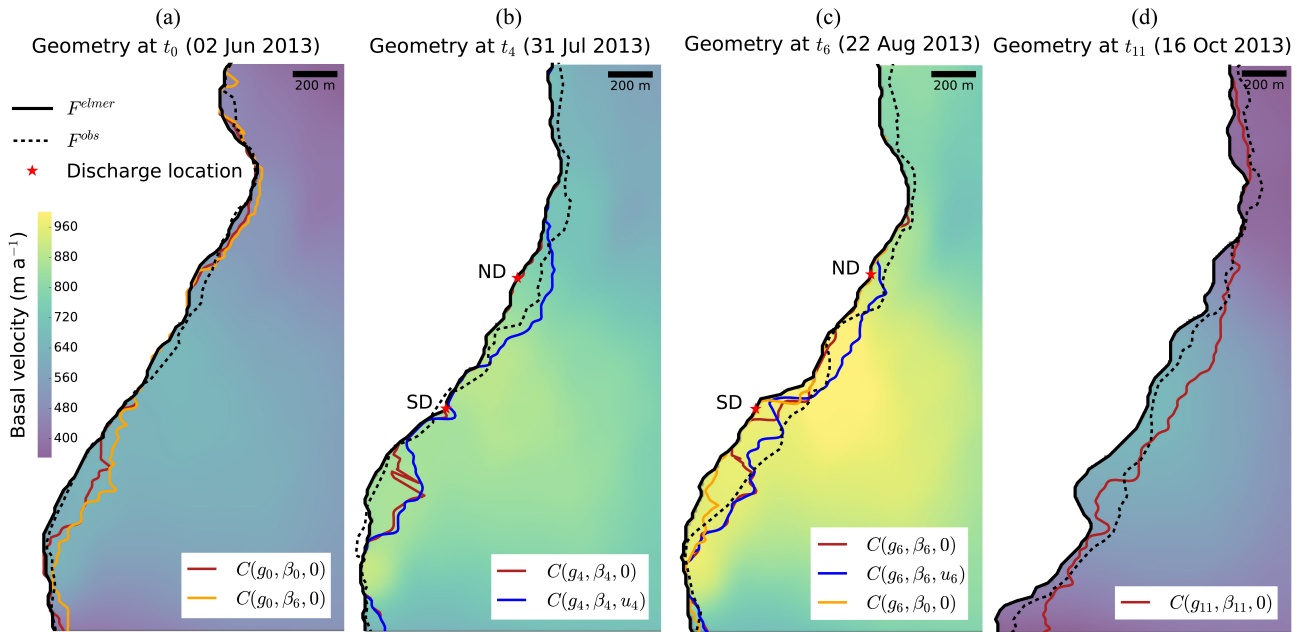
Figure 10. Basal velocity, advanced front before calving modelled with Elmer/Ice, F_i^{elmer}, at t_i in plain black, observed front after calving, F_i^{obs}, in dashed black and calving front modelled with HiDEM, F_i^{hidem} given the different configurations summarised in Table 2 for **(a)** $i = 0$, **(b)** $i = 4$, **(c)** $i = 6$, and **(d)** $i = 11$. Discharge locations (for $i = 4, 6$) are marked with a red star.

Vertical front configuration at t_6 (red line $C(g_6, \beta_6, 0)$ in Fig. 10c), during a period of accelerated glacier flow, results in slower modelled calving rate ($16.26 \times 10^5 \, \mathrm{m^3 \, d^{-1}}$) than observed ($26.94 \times 10^5 \, \mathrm{m^3 \, d^{-1}}$) and no front position change at both SD and ND leading to a mean distance to the observed front close to 60 m. With the undercut configuration (blue line $C(g_6, \beta_6, u_6)$ in Fig. 10b), modelled calving rate ($23.60 \times 10^5 \, \mathrm{m^3 \, d^{-1}}$) is similar to observation and the front positions at

5　discharge locations are reproduced even though the undercut only represents 5.2 % of the observed calving rate. The modelled front is still intensively breaking up south of SD but, at that date, it matches the observed retreat.

At the end of the melt season at t_{11}, when subglacial discharge has ended, the observed front retreats at a rate of $24.99 \times 10^5 \, \mathrm{m^3 \, d^{-1}}$ despite a frontal basal friction higher than at the last studied time step resulting to an averaged frontal velocity of $2.56 \times 10^5 \, \mathrm{m^3 \, d^{-1}}$. But as shown in Fig. 5, the sliding velocity is higher (lower basal friction, β_{11}) close to the front than further upglacier. Large

10　calving events occur at both former discharge locations where the bed elevation is lower than anywhere else. The calving front modelled by HiDEM (red line $C(g_{11}, \beta_{11}, 0)$ in Fig. 10d) manages to reproduce this behaviour but overestimates the retreat for the region in between, where the pattern of high strain rate is also denser (see Fig. 11).

Two configurations vary the friction coefficient, β, to assess the role of sliding in the calving process. If the basal friction is set according to t_6 and the geometry to t_0 (orange line $C(g_0, \beta_6, 0)$ in Fig. 10a), the calving rate exceeds observations by

15　more than a factor of 2 ($16.40 \times 10^5 \, \mathrm{m^3 \, d^{-1}}$), similar to $C(g_6, \beta_6, 0)$, yet with matching spatial frontal patterns as $C(g_0, \beta_0, 0)$ as well as strain rate distribution with elevated rates close to the calved zones. If the geometry of t_6 is simulated with the basal
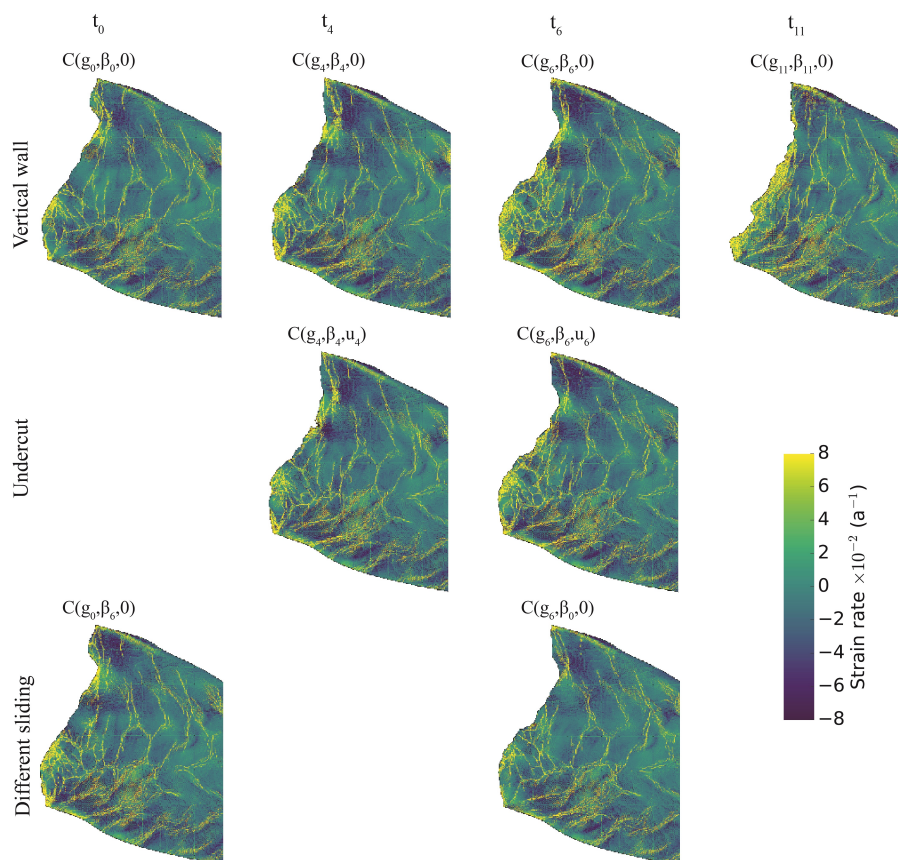
Figure 11. Strain rates modelled with HiDEM for each configuration. Yellow color shows the crevasse pattern and is denser close to the front where the difference between each configuration and time steps can be observed.

friction of t_0 (orange line $C(g_6, \beta_0, 0)$ in Fig. 10c), it is striking to notice again that the calved zones are similar to the vertical front configuration at t_6 but the calving rate is similar to the observed one at t_0. High strain rates are less pronounced than with the basal friction of t_6 but concentrated at the same locations.

5 Discussion

5.1 Plume Model and Undercutting

Our plume model uses a fixed, planar ice front to calculate submarine melt rates rather than a time-evolving geometry. This assumption is supported by Slater et al. (2017), who showed that the shape of the submerged ice front does not have a significant feedback effect on plume dynamics or submarine melt rates. However, the same study suggests that the total ablation driven

by submarine melting will increase due to the greater surface area available for melting. To take this effect into account in our undercut model, submarine melt rates are horizontally projected onto the undercut front modelled at the previous iteration.

The use of constant ambient ocean properties neglects inter- and intra-annual variability in Kongsfjorden. This variability may influence the plume through changes in the ambient density stratification, which affects both the vertical plume velocity

5 and neutral buoyancy height, and the temperature of ambient ocean water, which is linearly related to the melt rate. Due to this, there is some uncertainty in the relative magnitudes of the melt rate over longer time scales. However, the short-term variability of the plume-driven melt rate is dominated by changes in discharge during the melt season. This short-term variability determines the pattern of melt across the terminus and is therefore more significant for terminus morphology. A model based upon one-dimensional plume theory (e.g. Jenkins, 2011; Carroll et al., 2015; Slater et al., 2016) would be less

10 computationally expensive and may address some of these limitations; however, such a model would not capture the strong surface gravity currents driven by the plume and therefore would not accurately reproduce the spatial patterns of melt over short time scales which is important for the terminus morphology studied here.

For ND (Fig. 8b and d), the undercut is in line with the observed front to a certain extent, particularly for t_4. However, for SD, apart for t_3, no imminent correlation between modelled undercut and observed front location seems to exist. However,

15 Fig. 10 shows that modelling calving with undercut at SD and ND for t_4 and t_6 gives a good fit to observation. The difference in agreement with the observed front position and the modelled calving could possibly be explained by the uncertainty in discharge or the different character of the plume at high and low discharge. The low dependence of calving front position on modelled undercut in situations of low discharge seems to have no major influence on the performance of the calving model. At Kronebreen, the high discharge relative to the shallow depth of the terminus drives strong gravity currents at the surface

20 as water is rapidly exported horizontally away from the plume. The melt rates driven by these gravity currents are significant as shown in Fig. 7, and in some cases dominate over the melt rates driven by the plume at depth. The difference between low and high discharges is therefore slightly counter-intuitive. At low discharges, when maximum melt rates occur at depth, the terminus is more undercut but in a narrower area; meanwhile, at higher discharges, strong undercutting occurs but over a much wider area of the terminus. This suggests that calving behaviour may be very different in these two situations.

25 ## 5.2 Calving model

From our results we can conclude that undercutting by subglacial discharge is an essential factor for calving at discharge location. During the melt season (t_4 and t_6), surface melt leads to the formation of a subglacial drainage system that ultimately evacuates the water in the ocean from discharge points at the front of the glacier. Simulations without frontal undercutting at these subglacial discharge locations do not agree well with observed frontal positions and calving rates. In contrast, simulations

30 with frontal undercutting reproduce the retreat reasonably well at these locations and particularly where the discharge is high such as at ND. Nevertheless, higher subglacial discharge leading to increased undercutting does not necessarily result in larger retreat. For example, at t_6 (see Fig. 10c), the high discharge in ND enables a large undercut to be created close to the surface (see Fig. 8d), which ultimately triggers calving. However, the retreat at SD is larger despite lower discharge and smaller undercut (see Fig. 8e). Here the basal velocity is higher than at ND and probably plays a key role in the retreat since, even with a vertical

ice front, the glacier retreats. Besides, higher friction, β_0, leads to no retreat at all outlining the key role of basal friction. At t_4, on the other hand, with a similar undercut and higher basal friction, the observed front is advancing and the modelled front with undercut is slightly retreating. There is a fine tuning between basal friction and frontal undercutting magnitudes. At high discharge and high friction location (ND), frontal undercut seems to trigger calving primarily while at low discharge and low

5   friction location (SD), frontal undercut modulates the effects of basal friction on the calving process.

Moreover, calving modelling at t_0 and t_6 gives insight in the role of sliding and geometry (frontal position and topography) in the calving process. On one hand, the spatial distribution of the calved zones and the high strain rate regions are kept with similar geometries but different sliding. On the other hand, simulations with different geometries and similar basal friction show comparable calving rates. In this context, it appears that the geometry controls the calved zones while the basal friction

10   (glacier dynamics) controls the magnitude of calving (calving rate).

However, at t_{11}, with higher basal friction and no estimated subglacial discharge, hence no modelled undercut, the observed calving rate is still high ($24.99 \times 10^5 \, \mathrm{m^3 \, d^{-1}}$) compared to the start of the melt season. HiDEM manages to reproduce a high calving rate ($28.50 \times 10^5 \, \mathrm{m^3 \, d^{-1}}$) without taking neither the varying ocean temperature nor any undercut into account. This could be due to a combination of geometry and higher basal velocity at the front than inland (see Fig. 5d) leading to high

15   strain rates (see Fig. 11). In turn, the basal friction is a result of the basal hydrology of the region. Even when the melt season is finished, the drainage system is still influencing the dynamics and the calving. Luckman et al. (2015) showed that frontal ablation rates have the strongest correlation with ocean temperature in the fjord at the season timescale and the correlation with ice velocity appears when velocity is high. Our experiments are not including the varying fjord water temperature and limit our discussion on that subject but the velocity higher at the front than further inland seem in agreement with Luckman et al.

20   (2015)'s results.

In general, the calving rate is rather well reproduced under suitable conditions (undercut when appropriate and basal friction) apart from the simulation at t_4 where a large region, south of SD, is detached from the glacier in the model while the observed front is not changing. Different hypothesis can be suggested. First, the time between two observations, 26 days, is longer than for the other simulations, 11 days. During the melt season, the velocity can change drastically on a daily basis because of

25   surface runoff and subglacial drainage reorganisation. In this context, the basal friction for that time period is an average and since calving magnitude seems to be directly linked to basal velocity, the model might not reflect the real temporal evolution. In this sense, a smaller timestep could be a solution. However, the simulation at t_0 is also resulting in larger retreat than expected south of SD even though the timestep is smaller (11 days) and the basal friction during this period is not changing much. At t_6, this region is actually observed to be calving, reflected by model results. This zone of high strain rates was therefore expected to

30   calve but remained stable until that time while the calving model reproduces this retreat much earlier. Furthermore, in HiDEM, any block that is completely detached from the main ice body is considered as calved, even if only separated by a narrow crack from the rest of the glacier and still sitting at its original position. In this sense, HiDEM may model a calving earlier than observation as milimeter wide cracks would not be considered as calving by observations. In a full coupling, this effect would be neutralised if one is only interested at the accumulated ice loss over the whole season.

6   Conclusions

In this study, we use the abilities of different models to represent different glacier processes at Kronebreen, Svalbard with a focus on calving during the melt season of 2013. Observations of surface velocity, front position, topography, bathymetry and ocean properties were used to provide data for model inputs and validation.

5   The long-term fluid-like behaviour of ice is best represented using the continuum ice flow model Elmer/Ice that computes basal velocities by inverting observed surface velocities and evolves the geometry, including the front position. During the melt season, a subglacial hydrology system is created and the water is eventually evacuated at the front of the glacier. We used a simple hydrology model based on surface runoff directly transmitted to the bed and routing the basal water along the deepest gradient of the hydraulic potential. Two subglacial discharge locations have been identified by this approach: the northern one

10   evacuates water with a high rate ($\sim$10-100 $\mathrm{m^3\,s^{-1}}$) and the southern one with a low rate ($\sim$1-3 $\mathrm{m^3\,s^{-1}}$). This fresh water is subsequently mixed with ocean water. Rising meltwater plumes entrain warm fjord water and melts the subaqueous ice creating undercuts at the subglacial discharge location. We modelled the plume in 2D using a high-resolution plume model based upon the fluid dynamics code Fluidity adapted to the front height and the ocean properties of Kronebreen. Melt rates depend on the discharge rate and the shape of the plume differs greatly with its magnitude. Higher discharges tend to let the plume rise to the

15   surface close to which melt rates are the highest while low discharges concentrate the melt at lower elevations. The melt rates are then projected to the actual frontal geometry taking into account the subaqueous ice-front shape of the former timestep. It is interesting to note that modelled undercuts for high subglacial discharges are spatially close to the observed calving front whereas such a correspondence is not evident for small discharges. The elastic-brittle behaviour of the ice, such as crevasse formation and calving processes, is modelled using a discrete particle model, HiDEM. A new front position is calculated as

20   well as strain rates.

Four different factors impacting glacier calving are studied here through the calving model: geometry (topography and front position), basal sliding through basal friction, undercutting created by subglacial discharge and strain rate. The performance of the calving model is evaluated quantitatively by comparing observed and modelled calving rate and qualitatively by comparing calved regions. Results show that the high strain rate zones calculated by HiDEM seem to match the calved regions controlled

25   by the geometry even under modification of basal sliding. Basal friction, in turn, appears to control the magnitude of the retreat. Modelling undercut appears to be necessary to trigger calving at the subglacial discharge location, particularly at high discharge, but not sufficient as basal friction plays a role on the magnitude of the retreat.

This study confirms the controls on calving discussed by Benn et al. (2007) and goes further:

1. Geometry (frontal position and topography) controls the high strain rate locations and the calved regions,

30   2. Basal friction (associated to crevasse opening and glacier velocity) controls the calving rate,

3. Undercut, associated with geometry, subglacial drainage, and ocean properties, but also to former state of undercutting, controls the melt season calving at subglacial discharge locations, but undercuts created from high discharge have more

impact on the calving than from low discharge. High subglacial discharge concentrates the melt close to the water surface while low discharge creates an undercut at lower elevations.

To be able to perform a full coupling, a physical sliding law, depending on effective pressure at the bedrock, and consequently a more complex model describing the evolution of the subglacial hydrology, is needed. At this stage, the inversion helps to reproduce observed surface velocities with a given front position. If a new calving front from the model would be implemented, observed velocities would not necessarily match the new geometry.

References

Aliani, S., Sciascia, R., Conese, I., D'Angelo, A., Del Bianco, F., Giglio, F., Langone, L., and Miserocchi, S.: Characterization of seawater properties and ocean heat content in Kongsfjorden, Svalbard Archipelago, Rendiconti Lincei, 27, 155–162, doi:10.1007/s12210-016-0544-4, 2016.

Amundson, J. M. and Truffer, M.: A unifying framework for iceberg-calving models, Journal of Glaciology, 56, 822–830, doi:10.3189/002214310794457173, 2010.

Åström, J. A., Riikilä, T. I., Tallinen, T., Zwinger, T., Benn, D., Moore, J. C., and Timonen, J.: A particle based simulation model for glacier dynamics, Cryosphere, 7, 1591–1602, doi:10.5194/tc-7-1591-2013, 2013.

Åström, J. A., Vallot, D., Schäfer, M., Welty, E. Z., O'Neel, S., Bartholomaus, T., Liu, Y., Riikilä, T., Zwinger, T., Timonen, J., et al.: Termini of calving glaciers as self-organized critical systems, Nature Geoscience, 7, 874–878, doi:10.1038/NGEO2290, 2014.

Benn, D. I., Warren, C. R., and Mottram, R. H.: Calving processes and the dynamics of calving glaciers, Earth-Science Reviews, 82, 143–179, doi:10.1016/j.earscirev.2007.02.002, 2007.

Boehme, L., Lovell, P., Biuw, M., Roquet, F., Nicholson, J., Thorpe, S. E., Meredith, M. P., and Fedak, M.: Technical Note: Animal-borne CTD-Satellite Relay Data Loggers for real-time oceanographic data collection, Ocean Science, 5, 685–695, doi:10.5194/os-5-685-2009, 2009.

Carroll, D., Sutherland, D. A., Shroyer, E. L., Nash, J. D., Catania, G. A., and Stearns, L. A.: Modeling turbulent subglacial meltwater plumes: Implications for fjord-scale buoyancy-driven circulation, Journal of Physical Oceanography, 45, 2169–2185, doi:10.1175/JPO-D-15-0033.1, 2015.

Church, J., Clark, P., Cazenave, A., Gregory, J., Jevrejeva, S., Levermann, A., Merrifield, M., Milne, G., Nerem, R., Nunn, P., Payne, A., Pfeffer, W., Stammer, D., and Unnikrishnan, A.: Sea Level Change, book section 13, pp. 1137–1216, Cambridge University Press, Cambridge, United Kingdom and New York, NY, USA, doi:10.1017/CBO9781107415324.026, 2013.

Claremar, B., Obleitner, F., Reijmer, C., Pohjola, V., Waxegard, A., Karner, F., and Rutgersson, A.: Applying a Mesoscale Atmospheric Model to Svalbard Glaciers, Advances in Meteorology, Article ID: 321649, doi:10.1155/2012/321649, 2012.

Cook, S., Zwinger, T., Rutt, I., O'Neel, S., and Murray, T.: Testing the effect of water in crevasses on a physically based calving model, Annals of Glaciology, 53, 90–96, doi:10.3189/2012AoG60A107, 2012.

Cottier, F., Tverberg, V., Inall, M., Svendsen, H., Nilsen, F., and Griffiths, C.: Water mass modification in an Arctic fjord through cross-shelf exchange: The seasonal hydrography of Kongsfjorden, Svalbard, Journal of Geophysical Research: Oceans, 110, doi:10.1029/2004JC002757, 2005.

Darlington, E. F.: Meltwater delivery from the tidewater glacier Kronebreen to Kongsfjorden, Svalbard; insights from in-situ and remote-sensing analyses of sediment plumes, Ph.D. thesis, © Eleanor Darlington, 2015.

Everett, A., Lydersen, C., Kovacs, K. M., Kohler, J., and Sundfjord, A.: Hydrography data from GPS-CTD-SRDL-equipped Ringed seals in Kongsfjorden 2012, doi:10.21334/npolar.2017.7b538020, 2017.

Fried, M., Catania, G., Bartholomaus, T., Duncan, D., Davis, M., Stearns, L., Nash, J., Shroyer, E., and Sutherland, D.: Distributed subglacial discharge drives significant submarine melt at a Greenland tidewater glacier, Geophysical Research Letters, 42, 9328–9336, doi:10.1002/2015GL065806, 2015.

Gagliardini, O., Zwinger, T., Gillet-Chaulet, F., Durand, G., Favier, L., de Fleurian, B., Greve, R., Malinen, M., Martín, C., Råback, P., Ruokolainen, J., Sacchettini, M., Schäfer, M., Seddik, H., and Thies, J.: Capabilities and performance of Elmer/Ice, a new generation ice-sheet model, Geoscientific Model Development Discussions, 6, 1689–1741, doi:10.5194/gmdd-6-1689-2013, 2013.

Holland, D. M., Thomas, R. H., De Young, B., Ribergaard, M. H., and Lyberth, B.: Acceleration of Jakobshavn Isbrae triggered by warm subsurface ocean waters, Nature geoscience, 1, 659–664, doi:10.1038/ngeo316, 2008.

How, P., Benn, D. I., Hulton, N. R. J., Hubbard, B., Luckman, A., Sevestre, H., Van Pelt, W. J. J., Lïndback, K., Kohler, J., and Boot, W.: Rapidly-changing subglacial hydrology pathways at a tidewater glacier revealed through simultaneous observations of water pressure, supraglacial lakes, meltwater plumes and surface velocities, The Cryosphere Discussions, 2017, 1–29, doi:10.5194/tc-2017-74, 2017.

Howe, J. A., Moreton, S. G., Morri, C., and Morris, P.: Multibeam bathymetry and the depositional environments of Kongsfjorden and Krossfjorden, western Spitsbergen, Svalbard, Polar Research, 22, 301–316, doi:10.1111/j.1751-8369.2003.tb00114.x, 2003.

Jarrin, N., Benhamadouche, S., Laurence, D., and Prosser, R.: A synthetic-eddy-method for generating inflow conditions for large-eddy simulations, International Journal of Heat and Fluid Flow, 27, 585 – 593, doi:10.1016/j.ijheatfluidflow.2006.02.006, 2006.

Jenkins, A.: Convection-driven melting near the grounding lines of ice shelves and tidewater glaciers, Journal of Physical Oceanography, 41, 2279–2294, doi:10.1175/JPO-D-11-03.1, 2011.

Jenkins, A. and Bombosch, A.: Modeling the effects of frazil ice crystals on the dynamics and thermodynamics of Ice Shelf Water plumes, Journal of Geophysical Research: Oceans, 100, 6967–6981, doi:10.1029/94JC03227, 1995.

Kehrl, L. M., Hawley, R. L., Powell, R. D., and Brigham-Grette, J.: Glacimarine sedimentation processes at Kronebreen and Kongsvegen, Svalbard, Journal of Glaciology, 57, 841–847, doi:10.3189/002214311798043708, 2011.

Kimura, S., Candy, A. S., Holland, P. R., Piggott, M. D., and Jenkins, A.: Adaptation of an unstructured-mesh, finite-element ocean model to the simulation of ocean circulation beneath ice shelves, Ocean Modelling, 67, 39 – 51, doi:http://dx.doi.org/10.1016/j.ocemod.2013.03.004, 2013.

Köhler, A., Nuth, C., Kohler, J., Berthier, E., Weidle, C., and Schweitzer, J.: A 15 year record of frontal glacier ablation rates estimated from seismic data, Geophysical Research Letters, 43, doi:10.1002/2016GL070589, 2016.

Krug, J., Weiss, J., Gagliardini, O., and Durand, G.: Combining damage and fracture mechanics to model calving, The Cryosphere, 8, 2101–2117, doi:10.5194/tcd-8-1631-2014, 2014.

Krug, J., Durand, G., Gagliardini, O., and Weiss, J.: Modelling the impact of submarine frontal melting and ice mélange on glacier dynamics, The Cryosphere, 9, 989–1003, doi:10.5194/tc-9-989-2015, 2015.

Lindbäck, K., Kohler, J., Pettersson, R., Myhre, P. I., Nuth, C., Langley, K., Brandt, O., Messerli, A., and Vallot, D.: Subglacial topography, geology and implications for future bathymetry of Kongsfjorden, northwestern Svalbard, in preparation, 2017.

Luckman, A., Benn, D. I., Cottier, F., Bevan, S., Nilsen, F., and Inall, M.: Calving rates at tidewater glaciers vary strongly with ocean temperature, Nature communications, 6, doi:10.1038/ncomms9566, 2015.

McNabb, R., Hock, R., and Huss, M.: Variations in Alaska tidewater glacier frontal ablation, 1985–2013, Journal of Geophysical Research: Earth Surface, 120, 120–136, doi:10.1002/2014JF003276, 2015.

McPhee, M. G., Morison, J. H., and Nilsen, F.: Revisiting heat and salt exchange at the ice-ocean interface: Ocean flux and modeling considerations, Journal of Geophysical Research: Oceans, 113, doi:10.1029/2007JC004383, c06014, 2008.

Nahrgang, J., Varpe, Ø., Korshunova, E., Murzina, S., Hallanger, I. G., Vieweg, I., and Berge, J.: Gender specific reproductive strategies of an Arctic key species (Boreogadus saida) and implications of climate change, PLoS one, 9, e98 452, doi:10.1371/journal.pone.0098452, 2014.

Nick, F., Van der Veen, C. J., Vieli, A., and Benn, D.: A physically based calving model applied to marine outlet glaciers and implications for the glacier dynamics, Journal of Glaciology, 56, 781–794, doi:10.3189/002214310794457344, 2010.

Piggott, M. D., Gorman, G. J., Pain, C. C., Allison, P. A., Candy, A. S., Martin, B. T., and Wells, M. R.: A new computational framework for multi-scale ocean modelling based on adapting unstructured meshes, International Journal for Numerical Methods in Fluids, 56, 1003–1015, doi:10.1002/fld.1663, 2008.

Schellenberger, T., Dunse, T., Kääb, A., Kohler, J., and Reijmer, C. H.: Surface speed and frontal ablation of Kronebreen and Kongsbreen, NW Svalbard, from SAR offset tracking, The Cryosphere, 9, 2339–2355, doi:10.5194/tc-9-2339-2015, 2015.

Slater, D., Nienow, P., Goldberg, D., Cowton, T., and Sole, A.: A model for tidewater glacier undercutting by submarine melting, Geophysical Research Letters, 44, 2360–2368, doi:10.1002/2016GL072374, 2017.

Slater, D. A., Nienow, P. W., Cowton, T. R., Goldberg, D. N., and Sole, A. J.: Effect of near-terminus subglacial hydrology on tidewater glacier submarine melt rates, Geophysical Research Letters, 42, 2861–2868, doi:10.1002/2014GL062494, 2014GL062494, 2015.

Slater, D. A., Goldberg, D. N., Nienow, P. W., and Cowton, T. R.: Scalings for submarine melting at tidewater glaciers from buoyant plume theory, Journal of Physical Oceanography, 46, 1839–1855, doi:10.1175/JPO-D-15-0132.1, 2016.

Smagorinsky, J.: General circulation experiments with the primitive equations, Monthly Weather Review, 91, 99–164, doi:10.1175/1520-0493(1963)091<0099:GCEWTP>2.3.CO;2, 1963.

Straneo, F. and Heimbach, P.: North Atlantic warming and the retreat of Greenland's outlet glaciers, Nature, 504, 36–43, doi:10.1038/nature12854, 2013.

Tarboton, D. G., Bras, R. L., and Puente, C. E.: Combined hydrologic sampling criteria for rainfall and streamflow, Journal of Hydrology, 95, 323 – 339, doi:10.1016/0022-1694(87)90009-6, 1987.

Trusel, L. D., Powell, R., Cumpston, R., and Brigham-Grette, J.: Modern glacimarine processes and potential future behaviour of Kronebreen and Kongsvegen polythermal tidewater glaciers, Kongsfjorden, Svalbard, Geological Society, London, Special Publications, 344, 89–102, doi:10.1144/SP344.9, 2010.

Vallot, D., Pettersson, R., Luckman, A., Benn, D. I., Zwinger, T., Van Pelt, W., Kohler, J., Schäfer, M., Claremar, B., and Hulton, N. R. J.: Basal dynamics of Kronebreen, a fast-flowing tidewater glacier in Svalbard: global spatio-temporal response to water input, submitted to Journal of Glaciology in May 2017, 2017.

Van der Veen, C.: Calving glaciers, Progress in Physical Geography, 26, 96–122, doi:10.1191/0309133302pp327ra, 2002.

Van Pelt, W. J. J. and Kohler, J.: Modelling the long-term mass balance and firn evolution of glaciers around Kongsfjorden, Svalbard, Journal of Glaciology, 61, 731–744, doi:10.3189/2015JoG14J223, 2015.